iScience

CellPress
OPEN ACCESS

Article

Molecular structure of an amyloid fibril formed by FUS low-complexity domain

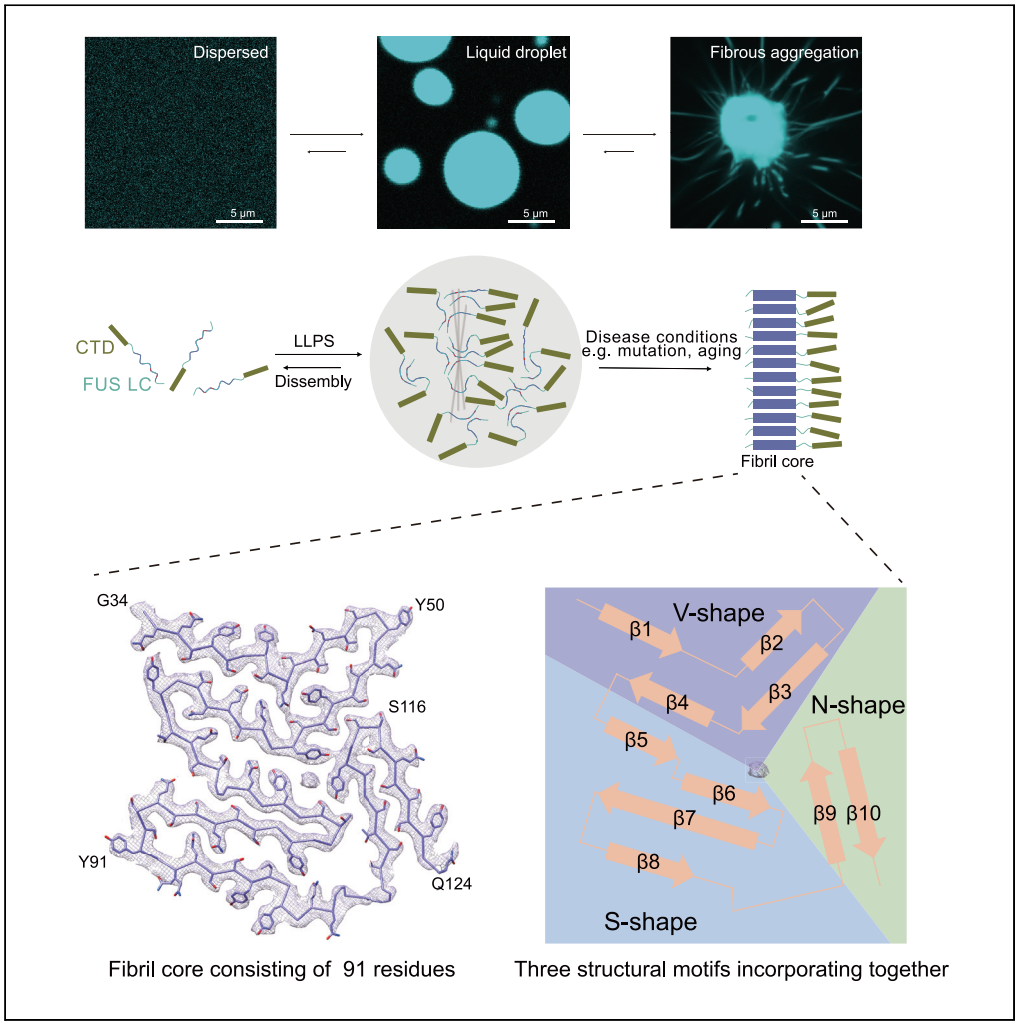

Yunpeng Sun, Shenqing Zhang, Jiaojiao Hu, ..., Qin Cao, Dan Li, Cong Liu

liulab@sioc.ac.cn

Highlights

Cryo-EM structure of an amyloid fibril formed by FUS low-complexity (LC) domain

FUS LC forms a novel enlarged and thermostable fibril core (FC) involving 91 residues

Hydrophilic interaction and hydrogen bonds are essential in FC formation of FUS LC

Sun et al., iScience 25, 103701
January 21, 2022
https://doi.org/10.1016/j.isci.2021.103701

iScience

CellPress
OPEN ACCESS

Article

Molecular structure of an amyloid fibril formed by FUS low-complexity domain

Yunpeng Sun,[1,2,6] Shenqing Zhang,[3,4,6] Jiaojiao Hu,[1,2,6] Youqi Tao,[3,4] Wencheng Xia,[1,2] Jinge Gu,[1,2] Yichen Li,[3,4] Qin Cao,[3] Dan Li,[3,4,5] and Cong Liu[1,7,*]

SUMMARY

FUS is a multifunctional nuclear protein which undergoes liquid–liquid phase separation in response to stress and DNA damage. Dysregulation of FUS dynamic phase separation leads to formation of pathological fibril closely associated with neurodegenerative diseases such as amyotrophic lateral sclerosis and frontotemporal dementia. In this study, we determined the cryo-EM structure of a cytotoxic fibril formed by the low-complexity (LC) domain of FUS at 2.9 Å resolution. The fibril structure exhibits a new and extensive serpentine fold consisting of three motifs incorporating together via a Tyr triad. FUS LC employs 91 residues to form an enlarged and stable fibril core via hydrophilic interaction and hydrogen bonds, which is distinct from most of previously determined fibrils commonly stabilized by hydrophobic interaction. Our work reveals the structural basis underlying formation of a cytotoxic and thermostable fibril of FUS LC and sheds light on understanding the liquid-to-solid phase transition of FUS in disease.

INTRODUCTION

Numerous amyloid proteins were found to form pathological amyloid aggregation which are closely related to neurodegenerative diseases (Eisenberg and Jucker, 2012; Soto and Pritzkow, 2018; Dobson et al., 2020; Qiang et al., 2017). Once formed under diseased condition, the pathological amyloid fibrils are highly stable (Iadanza et al., 2018; Sawaya et al., 2021). Moreover, the pathological fibrils formed by α-syn and Tau can self-propagate and spread from cell-to-cell involved in disease progression (Gambetti et al., 2011; Jucker and Walker, 2013; Kam et al., 2018; Peng et al., 2018, 2020; Vaquer-Alicea and Diamond, 2019). Extensive structural studies of amyloid fibrils reveal that hydrophobic and steric-zipper like interaction is important in determining the high stability of pathological fibrils (Paravastu et al., 2008; Eisenberg and Sawaya, 2017; Fitzpatrick et al., 2017; Gremer et al., 2017; Li et al., 2018; Li and Liu, 2021). Importantly, recent studies found that several RNA-binding proteins including fused in sarcoma (FUS), transactive response DNA-binding protein 43 kDa (TDP-43), and heterogeneous nuclear ribonucleoprotein A1 (hnRNPA1) can undergo liquid–liquid phase separation (LLPS) and form highly reversible amyloid fibrils mediated by the low-complexity amyloid-like kinked segments (LARKs) or reversible amyloid cores (RACs) which are dominated by hydrophilic interaction (Colombrita et al., 2009; Bentmann et al., 2012; Kato et al., 2012; March et al., 2016; Murray et al., 2017; Murray and Tycko, 2020; Guenther et al., 2018; Hughes et al., 2018; Luo et al., 2018; Gui et al., 2019; Sawaya et al., 2021). Moreover, prolonged stress or disease-mutation may promote the liquid-to-solid phase transition of these RNA-binding proteins to form highly stable fibrils which are believed to play a key role in the pathogenesis of amyotrophic lateral sclerosis (ALS) (Kim et al., 2013; Molliex et al., 2015; Murakami et al., 2015; Patel et al., 2015; Purice and Taylor, 2018; Cao et al., 2019; Gasset-Rosa et al., 2019; Sun et al., 2020; Portz et al., 2021). Structural investigation of the pathological fibrils formed by these proteins is important for understanding the liquid-to-solid phase transition of the RNA-binding proteins and its role in the related disease.

FUS is a nuclear protein playing key roles in the transcriptional regulation, RNA metabolism, and DNA damage response (Polymenidou et al., 2012; Schwartz et al., 2012; Wang et al., 2013; Deng et al., 2014; Yang et al., 2014; Rhoads et al., 2018). FUS is widely involved in RNA processing events including mRNA alternative splicing, nuclear exporting, miRNA metabolism, and stability of long noncoding RNAs (Wang et al.,

[1]Interdisciplinary Research Center on Biology and Chemistry, Shanghai Institute of Organic Chemistry, Chinese Academy of Sciences, Shanghai 201210, China

[2]University of the Chinese Academy of Sciences, Beijing 100049, China

[3]Bio-X Institutes, Key Laboratory for the Genetics of Developmental and Neuropsychiatric Disorders, Ministry of Education, Shanghai Jiao Tong University, Shanghai 200030, China

[4]Zhangjiang Institute for Advanced Study, Shanghai Jiao Tong University, Shanghai 200240, China

[5]Bio-X-Renji Hospital Research Center, Renji Hospital, School of Medicine, Shanghai Jiao Tong University, Shanghai 200240, China

[6]These authors contributed equally

[7]Lead contact

*Correspondence: liulab@sioc.ac.cn

https://doi.org/10.1016/j.isci.2021.103701

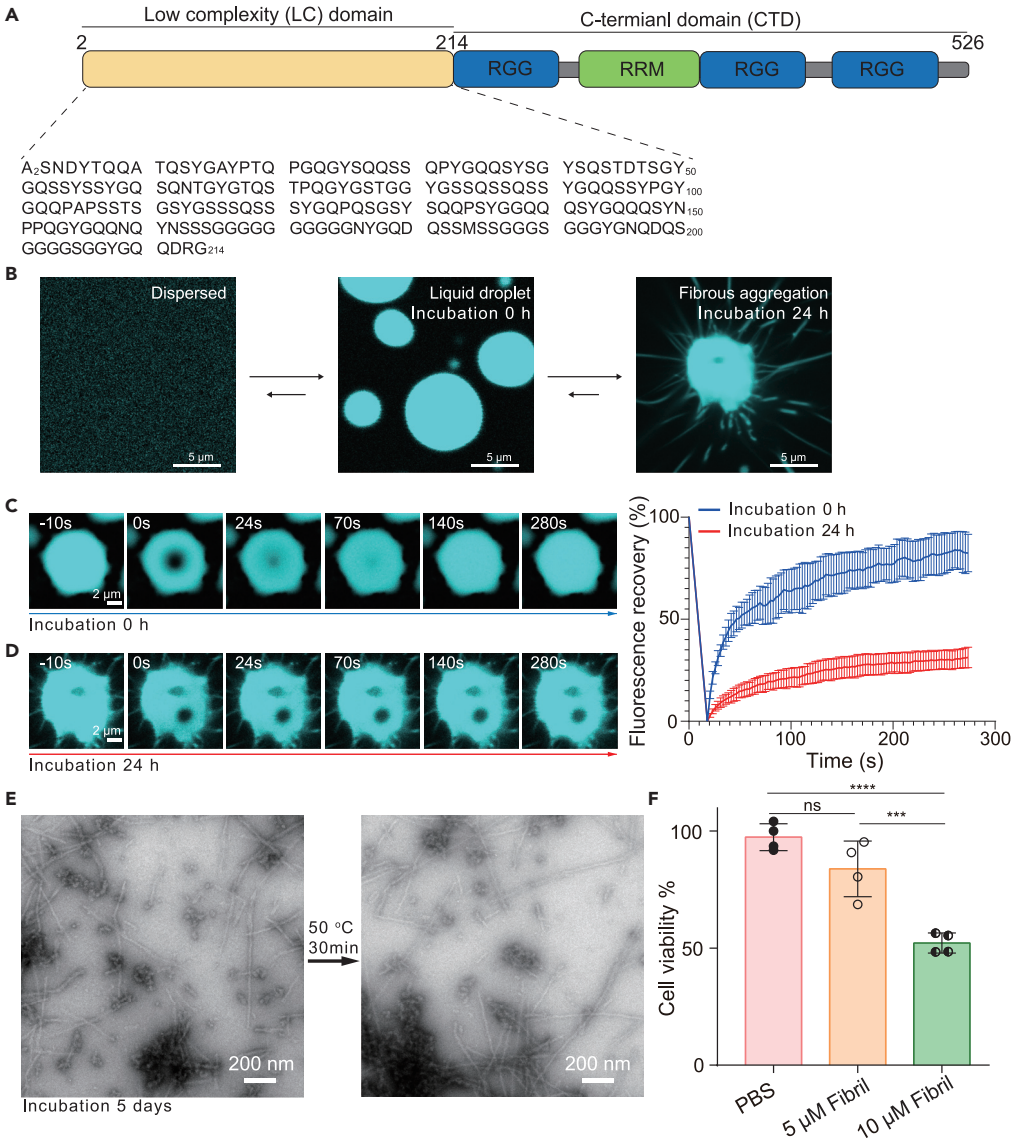

Figure 1. mCerulean-FUS LC forms liquid-droplet, and irreversible and cytotoxic fibril

(A) Domain organization of FUS. The sequence of FUS LC studied in this work is shown.

(B–D) Fluorescence images of FUS LC in different states. Scale bars, 5 μm. FRAP experiments of FUS LC droplets at 0 h (C) and irregular aggregates at 24 h (D). Scale bars, 2 μm. Data shown are means ± s.d., with n = 4 individual droplets.

(E) NS-TEM images of the fibrils formed by FUS LC (after 5 days of incubation) before and after 50°C heating. Scale bar: 200 nm.

(F) Cytotoxicity of the irreversible fibrils of FUS LC to HEK 293T cells measured by the CCK-8 kit assay. The concentration of FUS LC fibrils is indicated. Data are shown as mean ± S.D., with n = 4 biologically independent samples. ***p <0.001 (10μM Fibril vs. 5μM Fibril: 0.009); ****p <0.0001 (10μM Fibril vs. PBS: <0.0001); ns, not significant. One-way ANOVA followed by Tukey HSD post hoc test.

2008; Ju et al., 2011; Lagier-Tourenne et al., 2012; Ling et al., 2013; Fujii et al., 2005). FUS contains an N-terminal low-complexity (LC) domain, and a C-terminal domain (CTD) with one RNA recognition motif (RRM) and several arginine glycine-rich (RGG-rich) regions (Figure 1A). LC domain of FUS contains high percentage of Gly (24.88%), Ser (23.94%), Gln (20.19%), and Tyr (12.68%). Previous structural studies identified that the RAC1 (^{37}SYSGYS^{42}) and RAC2 (^{54}SYSSYG^{59}) within FUS LC is important in mediating both LLPS and highly reversible fibril formation of FUS LC (Luo et al., 2018). Moreover, solid-state nuclear magnetic resonance (ssNMR) study showed that residues 39–95 of FUS LC form a fibril core (FC_{type1}) mainly by hydrophilic interaction (Murray et al., 2017; Murray and Tycko, 2020).The same group recently reported a cryo-EM fibril

structure formed by the C-terminal half of FUS LC. In that structure, residues 112–150 form a U-shape fibril core (FC_{typeII}) (Lee et al., 2020). Notably, both full-length FUS and FUS LC can condense into highly stable fibril after several rounds of seeding growth, which can be significantly accelerated by ALS disease-related mutations (Kato et al., 2012; Murray et al., 2017; Ding et al., 2020; Patel et al., 2015). Therefore, structural study of formation of the highly stable FUS fibril is important for understanding the pathogenesis of FUS aggregation under diseased condition.

In this study, we determined the atomic structure of a highly stable fibrils formed by FUS LC by using cryo-electron microscopy (cryo-EM) at an overall resolution of 2.9 Å. The fibril structure contains an extensive and previously unobserved large fibril core ($FC_{typeIII}$) consisting of three structural motifs stabilized by hydrophilic interaction and a central Tyr triad layer. We further compared the cryo-EM structure of FUS LC fibrils with different FUS LC fibril structures previously determined. The structural analysis elucidates that the $FC_{typeIII}$ forms a larger FC by comprising a large segment (residues 98–124) of LC and rearranging the N-terminal regions including the two RACs, which provides structural understanding of the formation of a highly stable FUS LC fibril.

RESULTS

FUS LC forms irreversible and cytotoxic amyloid fibril

To investigate the liquid-to-solid phase transition and the fibril formation of FUS, we constructed mCerulean-FUS LC (residues 2–214, termed as FUS LC in short) and performed a maturation and aging assay of this construct (Figure 1A). FUS LC forms liquid-like droplet instantly upon adding dextran as crowding reagent (Figure 1B). Fluorescence recovery after photobleaching (FRAP) assay showed that the intensity of the fresh prepared FUS LC droplets (0 h incubation) rapidly recover in 280 s, demonstrating the high interior dynamics and liquid-like property of FUS LC droplet (Figures 1B and 1C). In contrast, upon further incubation for 24h, FUS LC forms fibrillar structures protruding from the droplets (Figure 1B). FRAP results showed that the dynamic property of FUS LC losses dramatically in the matured droplet (Figure 1D), suggesting a liquid-to-solid phase transition of FUS LC.

To obtain substantial amount of the FUS LC fibril samples for further cytotoxicity and structural characterization, we incubated FUS LC for 5 days at 37°C and harvested the fibrils. By using negative-staining transmission electron microscopy (NS-TEM), we confirmed that FUS LC forms typical amyloid fibrils which are highly thermostable without obvious dissociation even being heated to 50°C for 30 min (Figure 1E). Remarkably, the thermostable FUS LC fibril exhibits potent cytotoxicity to HEK293T cells in a dose-dependent manner, implying the potential pathological relevance of the FUS LC fibril (Figure 1F). Together, our results show that FUS LC undergoes liquid-to-solid phase transition and forms cytotoxic and thermostable fibrils.

Cryo-EM structure determination of the amyloid fibril formed by FUS LC

We next performed cryo-EM to determine the atomic structure of the FUS LC fibrils. Firstly, the preformed thermostable fibrils were fixed on a carbon grid and frozen in liquid ethane. Then, the cryo-EM data were collected by using a Gatan K2 Summit camera on a Titan Krios transmission electron microscope. 16,394 fibrils from 1,089 micrographs were selected for the reconstruction of FUS LC fibril (Figure 2A and Table 1). Only one dominant species of twist fibril with a population of over 99% were identified through two-dimensional (2D) classification with a 1,024-pixel box size (Figure 2B). Finally, we reconstructed a three-dimensional (3D) density map of FUS LC to an overall resolution of 2.9 Å at 0.143 cutoff of Fourier shell correlation (FSC) by performing helical reconstruction using RELION3.1(Scheres, 2020) (Figures 2C and S1). According to the density map, the fibril consists of a single protofilament where FUS LC subunits stack on top of each other along the fibril axis. The fibril features a left-handed helix with a full pitch of ~125 nm, a helical twist of −1.44°, and a helical rise of 5.0 Å (Figure 2D and Table 1).

Overall structure of the $FC_{typeIII}$ of FUS LC

Based on the high-quality cryo-EM density map, we were able to build an atomic model of the $FC_{typeIII}$ of FUS LC fibril unambiguously. $FC_{typeIII}$ of FUS LC is composed of residues 34–124 (Figure 3A), which form ten individual β-strands (β1–β10) arranging into a large serpentine fold (Figure 3B). The N-terminal fused His-tagged mCerulean protein (29.9 kDa) is not involved in the structure of $FC_{typeIII}$. For each subunit, β2–β6 and β8–β9 are in the same layer (i), whereas strands β1, β7, and β10 swap up to (i+1/2) layer to interact

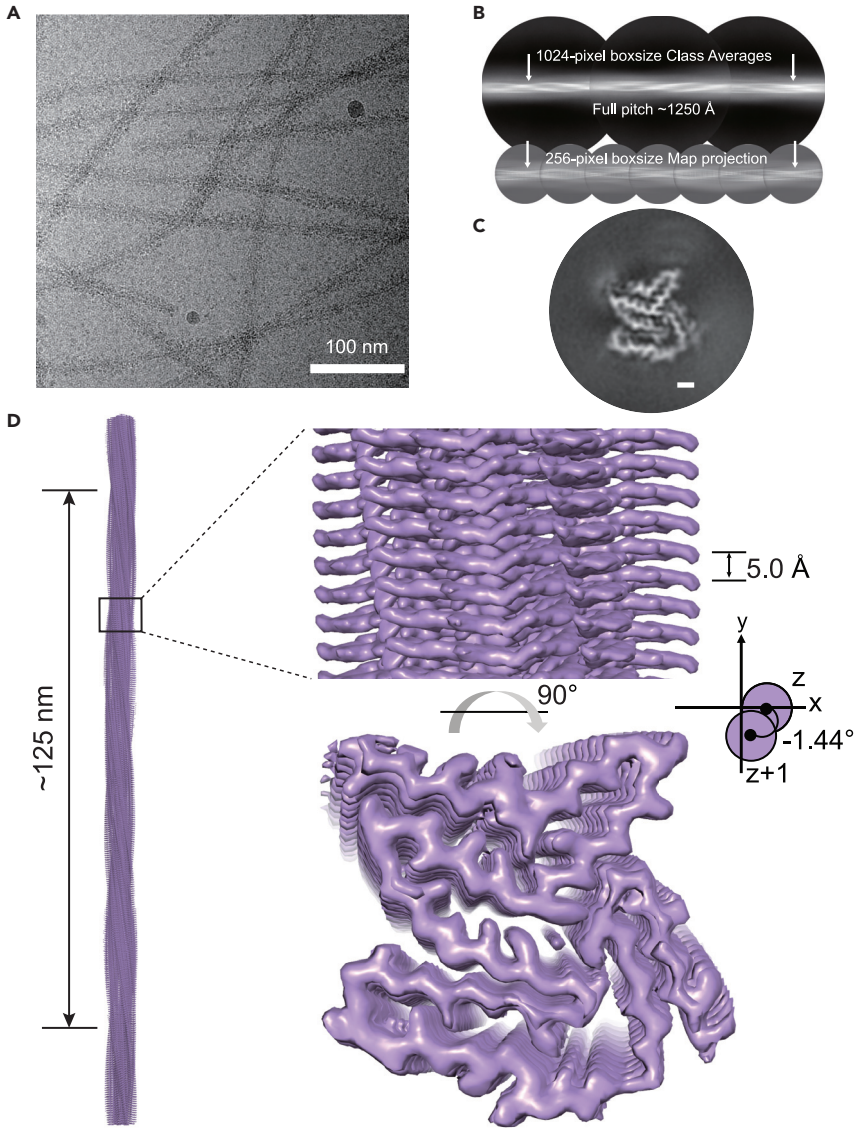

Figure 2. Cryo-EM structure determination of the FUS LC fibril

(A) Cryo-EM image of the irreversible fibrils formed by FUS LC. Scale bar: 100 nm.

(B) 2D class averages (box size: 1,024 pixels) used to calculate crossover distance and map projections (box size: 256 pixels) match 2D class averages.

(C) A central slice from the 3D reconstruction of FUS LC fibril. Scale bar: 1nm.

(D) Cryo-EM density map of the FUS LC fibril. Fibril parameters including half pitch, twist angle, and rise are labeled. See also Figure S1.

with β4, β6, β8, and β9 from neighboring subunits in the layer (i) and (i+1), respectively (Figure S2). The $FC_{typeIII}$ can be divided into three structural motifs, including the N-terminal V-shape motif consisting of β1–β4, the middle S-shape motif consisting of β5–β8, and the C-terminal N-shape motif formed by β9–β10 (Figure 3C). Strikingly, the central interface of three motifs is formed by a Tyr triad (Y58, Y75, and Y113, each from one motif). The aromatic side chains of Tyr form π–π interactions for stabilizing the interface. In addition, an ordered solvent molecule is localized in the center of the Tyr triad (Figure 3C).

The $FC_{typeIII}$ of FUS LC is formed predominantly by Tyr, Gln, Ser, Gly, and Thr, but not hydrophobic residues such as Val, Leu, and Ile which are often observed in the structure of pathological FC previously determined (Figure 3D). Notably, each of the three motifs is formed by zipper-like interaction (Figure 3E). The interfaces are mainly formed by hydrophilic interaction by Gln and Ser (Figures 3C and 3E). Specifically, in the V-shape

Table 1. Statistics of cryo-EM data collection and refinement

Name	FUS LC fibril
PDB ID	7VQQ
EMDB ID	EMD-32092
Data collection	
Pixel size (Å)	1.1
Defocus Range (μm)	−2 to −1
Voltage (kV)	300
Camera	K2 summit
Microscope	Titan Krios
Exposure time (s/frame)	0.19
Number of frames	32
Total dose ($e^-/Å^2$)	40
Reconstruction	
Micrographs	1,089
Manually picked fibrils	16,394
Box size (pixel)	256
Inter-box distance (Å)	28.2
Segments extracted	381,229
Segments after Class2D	276,426
Segments after Class3D	171,163
Resolution (Å)	2.9
Map sharpening B-factor ($Å^2$)	−104.169
Helical rise (Å)	5.0
Helical twist (°)	−1.44
Atomic model	
Non-hydrogen atoms	1,971
Protein residues	273
Ligands	0
r.m.s.d. Bond lengths	0.009
r.m.s.d. Bond angles	0.847
All-atom clash score	2.49
Rotamer outliers	0.00%
Ramachandran outliers	0.00%
Ramachandran allowed	12.36%
Ramachandran favored	87.64%

motif, β1–β4 forms a hydrophilic interface by the side chains of Gln, Ser, Tyr, and Thr (Q35, S37, S39, S42, Q43, T45, T47, S53, Y55, S57, Q60, Q62, T64, and Y66) (Figures 3C and 3E). Residues 67–97 constitute an S-shape motif (strands β5–β8) including a β-hairpin structure composed of strands β7–β8 which is stabilized by the hydrophilic interaction of Gln and Ser. The C-terminal N-shape motif features a β-hairpin structure. Six Ser residues (S108, S110, S112, S117, S119, and S121) align into a zipper-like architecture and form a hydrophilic interface (Figure 3E). Thus, Ser and Gln are essential in forming the hydrophilic interface of the $FC_{typeIII}$ of FUS LC.

In addition to Ser and Gln, there are 13 Tyr residues in the $FC_{typeIII}$. Among them, Y58, Y75, and Y113 form a Tyr triad in the center of $FC_{typeIII}$ and stabilize the three motifs via π–π interaction (Figures 3C and 3F). Y55 and Y81 are on the edge of zipper-like interface and form hydrogen bonds with Q43 and Q102, respectively. Y55 is involved in the formation of zipper-like interface. The rest of Tyr residues including Y38, Y41, Y50, Y66, Y91, Y97, Y100, and Y122, faces outside of the $FC_{typeIII}$ with the side chain exposing to the

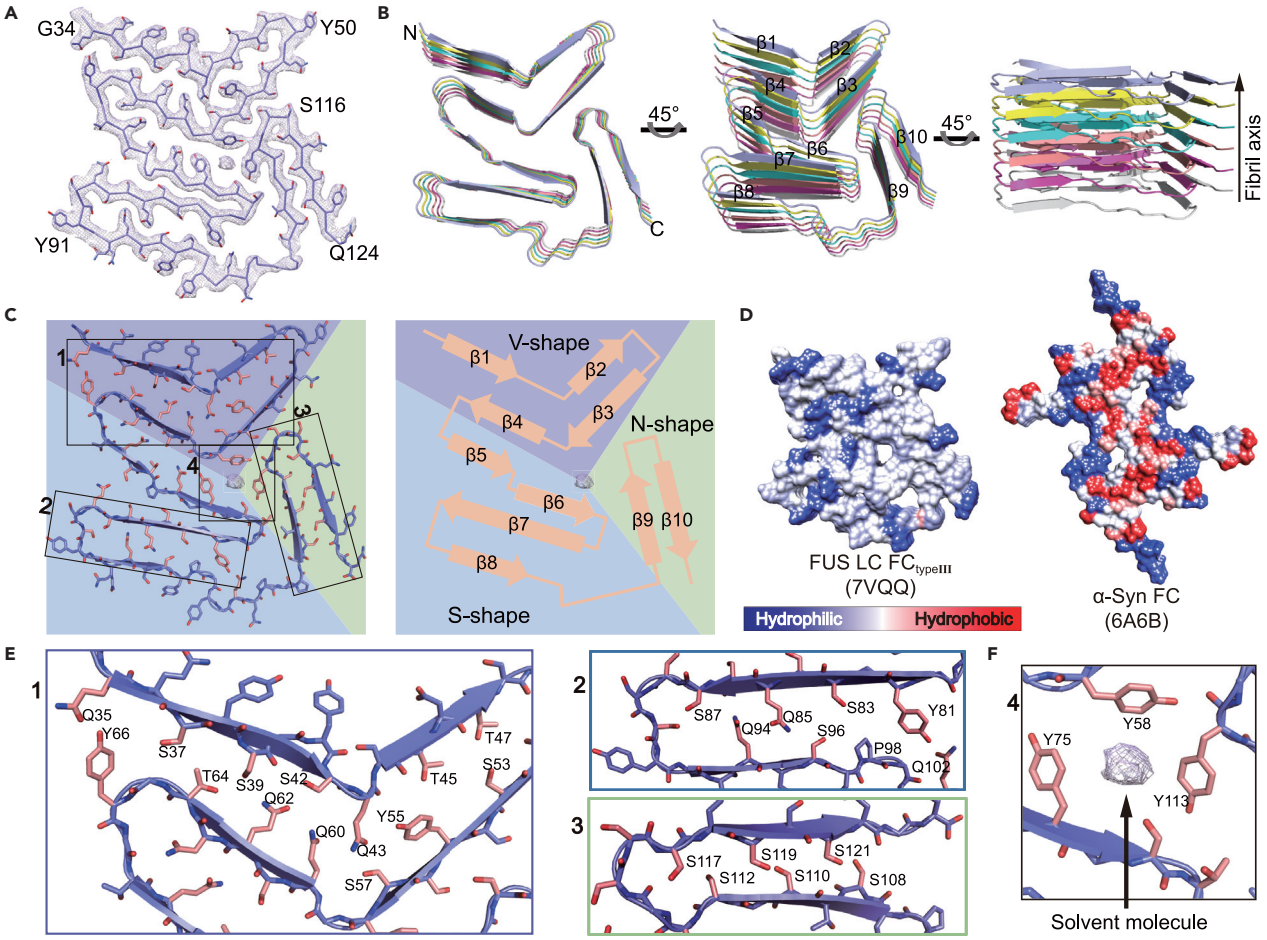

Figure 3. Overall structure of the FUS LC fibril

(A) Density map and the structure model of one cross-sectional layer of the FUS LC fibril.

(B) Views of six layers of FUS LC fibril are shown in cartoon. The fibril axis is indicated. The β-strands are numbered and labeled accordingly.

(C) Top view of structure model of one subunit of FUS LC fibril (left). Cartoons on the right show topology of the subunit. Three structural motifs are present. The N-terminal region is stabilized by the V-shape motif (purple) comprising of β1–β4. The S-shape motif (blue) and the N-shape motif (green) are stabilized mainly by zipper-like hydrophilic interactions involving side chains within strands β5–β8 and β9–β10, respectively. Side chains of residues involved in zipper-like interactions are colored in salmon.

(D) The surfaces of one subunit of FUS LC $FC_{typeIII}$ and one polymorphic structure of α-syn FC are shown according to the hydrophobicity of the residues. PDB IDs of the structures including FUS LC $FC_{typeIII}$ and α-syn FC are provided in parentheses.

(E) Zoom-in views of the V-shape motif and two β-hairpin structures formed by β7–β8 and β9–β10 in S-shape and N-shape motif, respectively.

(F) Zoom-in view of the Tyr triad buried in the center of FUS LC fibril. The density of the unidentified solvent molecule in the center of the Tyr triad is marked.

See also Figures S2 and S3.

solvent (Figure S3). Together, the cryo-EM structure demonstrated that FUS LC consists of three motifs stabilized by hydrophilic interaction which is mainly contributed by Ser and Gln. The three motifs are assembled together by a Tyr triad.

Structural comparison of different fibril structures of FUS LC

We next compared the cryo-EM structure of the thermostable fibril of FUS LC to the other three structures formed by different segments of FUS LC (Figure 4A). We previously determined the two RACs of FUS LC comprising of tandem (S/G)Y(S/G) motifs: RAC1 (^{37}SYSGYS^{42}) and RAC2 (^{54}SYSSYG^{59})(Luo et al., 2018). The RACs structures feature ordered-coil hydrophilic and hydrous interfaces which accounts for their high instability (Figure 4B). Remarkably, these two RACs rearrange and form extended hydrophilic zipper-like structures with Tyr, Gln, Thr, and Ser (Q35, S37, S39, S42, Q43, Q60, T64, Y66) in the V-shape motif in the $FC_{typeIII}$ (Figures 4C and 4D). Moreover, the β-turn region (residues 113–116) from N-shape

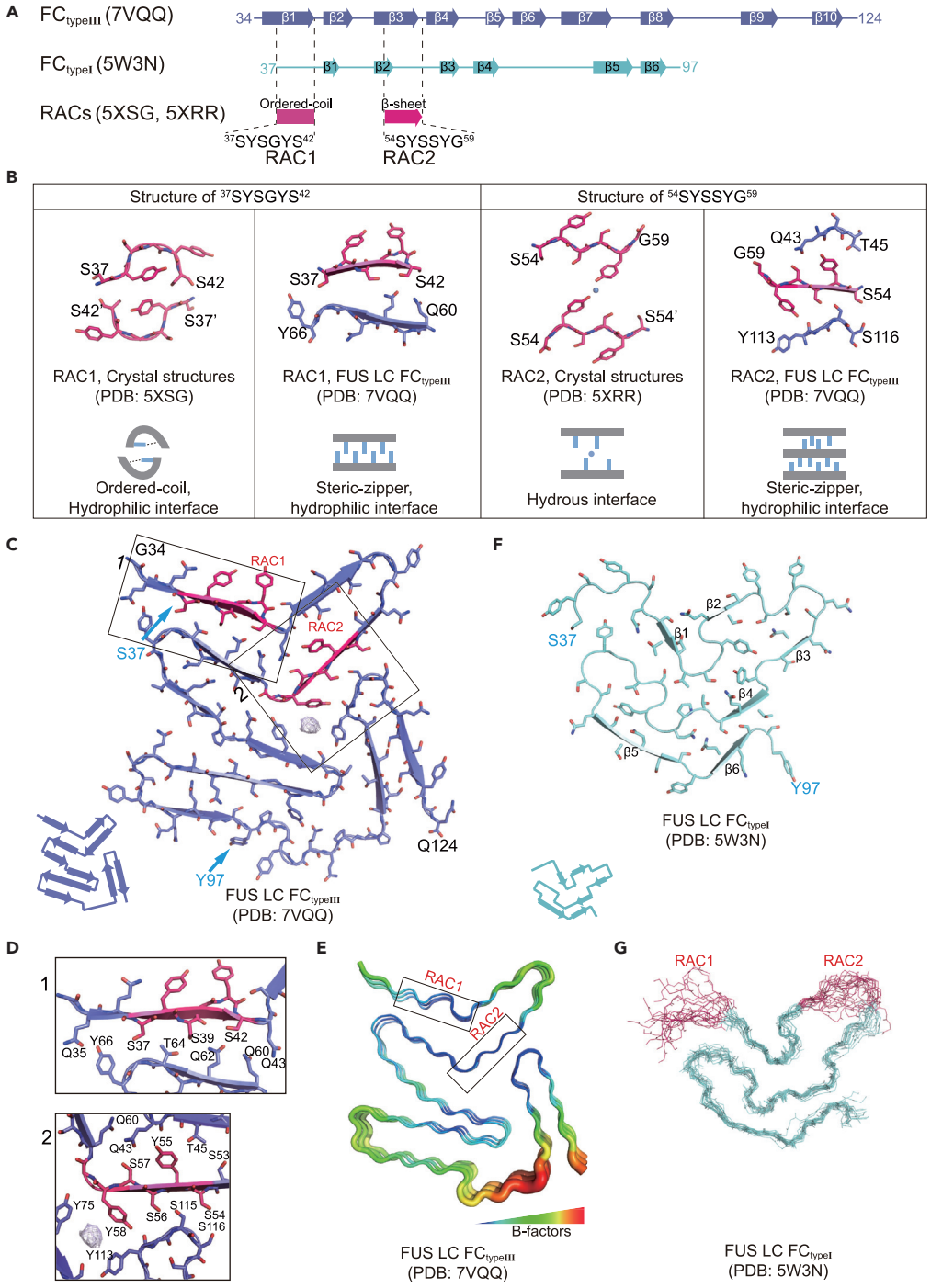

Figure 4. Comparison of different structures of FUS LC fibrils

(A) The sequence involved in the formation of the two RACs, $FC_{typeIII}$, and FC_{typeI} are mapped with the secondary structured highlighted.

(B) The structures of the two RACs in the reversible RACs structures (left) and in the $FC_{typeIII}$ (right). The structure cartoons are shown in the bottom.

(C) Structure model of a single subunit of the $FC_{typeIII}$. The topology diagram is shown in the bottom. The two RACs are boxed and highlighted in red.

(D) Zoomed-in view is shown in (D).

Figure 4. *Continued*
(E) The B-factor putty of the three layers of $FC_{typeIII}$ is shown. The two RACs shown in the box feature low B-factor compared to the other regions of the $FC_{typeIII}$.
(F) The structure model of one FUS LC subunit in FC_{typeI}. The topology diagram is shown in the bottom.
(G) Superposition of the 20 low-energy models of FC_{typeI} shows highly dynamic property of the two RACs. RACs are colored in red. PDB IDs of the structures including two RACs crystal structures, $FC_{typeIII}$, and FC_{typeI} are provided in parentheses.
See also Figures S4 and S5.

motif interacts with and stabilizes RAC2 in the $FC_{typeIII}$ (Figure 4D). The relatively low B-factor of the two RACs suggests that they are highly stable in the $FC_{typeIII}$ (Figure 4E).

In addition to RAC1 and RAC2, an ssNMR structure of FC_{typeI} formed by FUS LC was reported (Murray et al., 2017). We next compared the structure of FC_{typeI} and $FC_{typeIII}$. The FC_{typeI} consists of residues 39–95 which form 6 β-strands and folds into a relatively smaller serpentine fold distinct from that of the $FC_{typeIII}$ (Figures 4A and 4F). Specifically, residues 98–124 which form the N-shape motif of the $FC_{typeIII}$ remain flexible and are not involved in the formation of the FC_{typeI} (Figures 4C and 4F). Moreover, the RAC1 and RAC2 are dynamic with high flexibility in the FC_{typeI} as demonstrated by the superposition of the 20 low-energy structural models of FC_{typeI} (Figure 4G). Notably, D46, the only charged residue in both the FC_{typeI} and the $FC_{typeIII}$, is excluded from the interior of the $FC_{typeIII}$ and is completely solvent-exposed (Figure S4A). Whereas, in the 20 low-energy structural models of FC_{typeI}, the side chain of D46 partially folds into the interior of FC_{typeI} and interacts with S44 and Q52 (Figure S4B). Altogether, the structural analysis suggests that FUS LC incorporates the large segment (residues 98–124) as well as rearranges the N-terminal region (residues 34–97) including the RACs to form a larger and more stable $FC_{typeIII}$.

DISCUSSION

FUS can form highly dynamic liquid-like droplet involved in stress granule formation (Portz et al., 2021; Murakami et al., 2015). Under aging and diseased condition, FUS can further condense into thermostable amyloid fibrils which are closely associated with ALS and frontotemporal dementia (Patel et al., 2015; Kato et al., 2012). Previous work showed that multiple Tyr residues from the (S/G)Y(S/G) motifs of FUS LC may form π–π interaction to mediate FUS LC LLPS(Martin et al., 2020). Meanwhile, FUS LC may use the two tandem (S/G)Y(S/G) motifs (RAC1 and RAC2) to form highly unstable amyloid fibrils (Luo et al., 2018). Moreover, FUS LC can use its N-terminal residues 39–95 to form a hydrophilic FC_{typeI} (Murray et al., 2017; Murray and Tycko, 2020). While, incorporating residues 97–124 into the FC structurally rearranges the entire FUS LC to form a much larger and stable $FC_{typeIII}$, resulting in the formation of thermostable fibril of FUS LC as observed in this study (Figures 1E and 3A). In additional to the N-terminal of FUS LC, a recent study reported that the C-terminal half (residues 111–214) of FUS LC can form amyloid fibril with a U-shape architecture (FC_{typeII}) which is distinct from those formed by the mCerulean-FUS LC construct ($FC_{typeIII}$) (Figure S5). These structural studies demonstrate that, under different condition, FUS may utilize different regions of LC to form different types of intra- and intermolecular interactions, which enables FUS to form different molecular assembles including liquid-like droplets and distinct fibril polymorphs (Kato et al., 2012; Luo et al., 2018; Murray et al., 2017; Patel et al., 2015; Murakami et al., 2015). However, several key questions remain to be explored, including (1) whether FUS LC forms the same $FC_{typeIII}$ structure in the context of the full-length FUS as that fused with mCerulean (Figure S5A), (2) whether these different fibril structures of FUS LC determined *in vitro* are indeed exist in cells, and (3) how these different structures interconvert and are regulated under normal or disease conditions.

Recent advances in cryo-EM results in rapid accumulation of pathological amyloid fibrils structures formed by different proteins including Tau, α-syn, and human PrP (Shi et al., 2021; Schweighauser et al., 2020; Wang et al., 2020; Iadanza et al., 2018; Li et al., 2018). These fibril structures demonstrate that hydrophobic interaction serves as one of the major driving forces for stabilizing the fibrils which are normally very stable once formed (Sawaya et al., 2021; Dobson et al., 2020). Whereas, in this study, we showed that hydrophilic interaction is dominated in the structure of the thermostable fibril of FUS LC. Strikingly, FUS LC uses nearly 90 residues to form an extensive $FC_{typeIII}$, which is larger than most of FC of the single protofilament from the pathological fibrils and FUS LC FC_{typeI} previously determined (Figure 5A). Thus, despite that FUS LC can only form less stable hydrophilic interaction within the FC which may play an important role in mediating dynamic assembly of FUS LC (Figure 4F), it may still form thermostable fibril by incorporating a large number of residues to build up a larger and more stable FC (Figure 5B). Furthermore, the large FC is stabilized by several hydrophilic zipper-like interaction within the three motifs and excludes the charged residue from

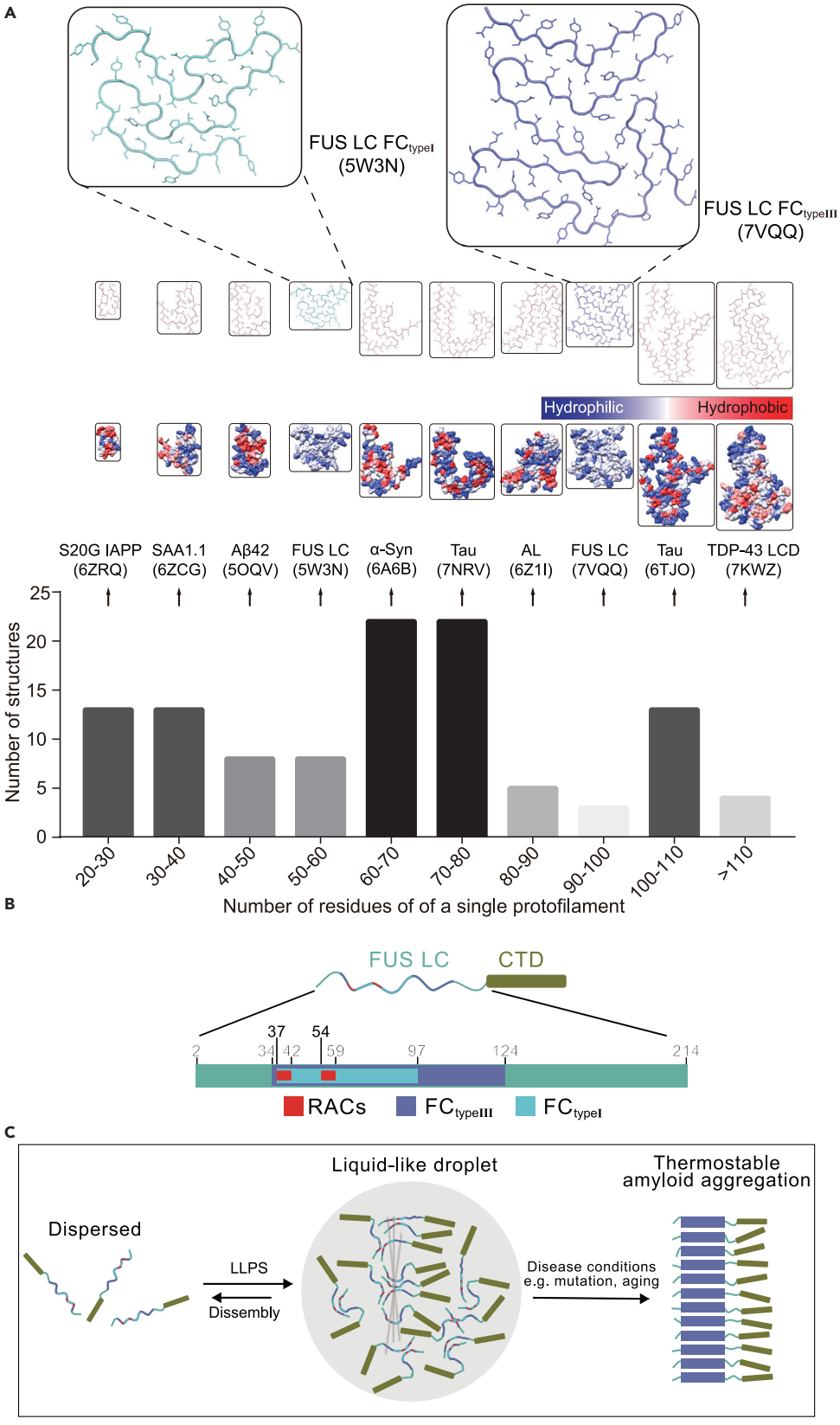
A
FUS LC FC typeI (5W3N)
FUS LC FC typeIII (7VQQ)
Hydrophilic
Hydrophobic
S20G IAPP (6ZRQ)
SAA1.1 (6ZCG)
Aβ42 (5OQV)
FUS LC (5W3N)
α-Syn (6A6B)
Tau (7NRV)
AL (6Z1I)
FUS LC (7VQQ)
Tau (6TJO)
TDP-43 LCD (7KWZ)
Number of structures
0
5
10
15
20
25
20-30
30-40
40-50
50-60
60-70
70-80
80-90
90-100
100-110
>110
Number of residues of of a single protofilament
B
FUS LC
CTD
37
54
2
34
42
59
97
124
214
RACs
FC typeIII
FC typeI
C
Liquid-like droplet
Thermostable amyloid aggregation
Dispersed
LLPS
Dissembly
Disease conditions e.g. mutation, aging

Figure 5. Structural analysis of fibrils formed by FUS LC and other proteins, and the diagram illustration of the potential conversion of FUS LC between different states

(A) Distribution of FC residues numbers (of a single protofilament) from 100 different cryo-EM amyloid fibril structures (the full list of the PDB codes of the fibril structures are listed in data and code availability). The surface hydrophobicity of the representative FC structures from different subgroups is shown. The structure models of both $FC_{typeIII}$ and FC_{typeI} are highlighted. PDB IDs of the representative FC structures are provided in parentheses.

(B) Domain organization of FUS. Different regions of FUS LC identified to form FC in different fibril structures are colored. Specifically, residues 34–124 that are involved in $FC_{typeIII}$ are colored in slate. Residues 37–97 that are involved in the structural model of FC_{typeI} is colored in cyan. The two RACs segments are highlighted in red.

(C) Schematic illustration of different states of FUS. FUS LC is highly dynamic in monomeric state. The RACs and FC_{typeI} may play important roles in mediating FUS LC dynamic assembly in the reversible phase separated state. Under pathological conditions, FUS LC may further assemble into irreversible amyloid fibrils by forming the $FC_{typeIII}$.

the interior of FC, which both contribute to the increased fibril thermostability. Thus, our structural study provides insight into understanding the high diversity of amino acid composition and driving force for forming thermostable amyloid fibrils with different fibril polymorphs.

Limitations of the study

This study reveals a cryo-EM structure of a cytotoxic and thermostable amyloid fibril formed by the FUS LC. The limitation is that the FUS LC construct used in this study contains an N-terminal mCerulean tag, which is relatively large and may influence the packing of FUS LC in fibrils. Whether FUS LC forms the same $FC_{typeIII}$ structure (1) in the absence of the N-terminal fusion tag and (2) in the context of the full-length FUS need be further explored.

STAR★METHODS

Detailed methods are provided in the online version of this paper and include the following:

- KEY RESOURCES TABLE
- RESOURCE AVAILABILITY
  - Lead contact
  - Materials availability
  - Data and code availability
- METHOD DETAILS
  - Purification of recombinant mCerulean-FUS LC
  - Fluorescence recovery after photo bleaching (FRAP) assay and fibril formation
  - Cell viability assay
  - Negative-staining transmission electron microscopy
  - Cryo-EM data collection
  - Imaging processing, reconstruction, and model building
  - Atomic model building
- QUANTIFICATION AND STATISTICAL ANALYSIS

SUPPLEMENTAL INFORMATION

Supplemental information can be found online at https://doi.org/10.1016/j.isci.2021.103701.

ACKNOWLEDGMENTS

This work was supported by the National Natural Science Foundation of China (NSF) of China (82188101, 32171236 and 31872716 to C.L.; 32170683 to D.L.), the Major State Basic Research Development Program (2019YFE0120600 to C.L.), the Science and Technology Commission of Shanghai Municipality (STCSM) (Grant No. 20XD1425000 and 2019SHZDZX02 to C.L.), the CAS project for Young Scientists in Basic research (Grant No.YSBR-009 to C.L.), the "Eastern Scholar" project supported by the Shanghai Municipal Education Commission to D.L, and the Joint Funds of the National Natural Science Foundation of China (key program no. U1932204). We would like to thank for data collection in the Instrument Analysis Center (IAC), Shanghai Jiao Tong University on Cryo-EM.

AUTHOR CONTRIBUTIONS

Y.S., D.L., and C.L. designed the project. Y.S., S.Z., and J.H. prepared fibril samples and performed the biochemical assays. Y.S. prepared cryo-EM samples and performed cryo-EM data collection and processing. S.Z. performed the FRAP assay. J.H. performed the cell viability assay. W.X., Y.T., and Q.C. assisted in cryo-EM data collection and processing. J.G. and Y.L. assisted in protein purification. All of the authors are involved in analyzing the data and contributed to manuscript discussion and editing. Y.S., D.L., and C.L. wrote the manuscript.

DECLARATION OF INTERESTS

The authors declare no competing interests.

Received: October 25, 2021
Revised: November 22, 2021
Accepted: December 22, 2021
Published: January 21, 2022

REFERENCES

Adams, P.D., Afonine, P.V., Bunkoczi, G., Chen, V.B., Davis, I.W., Echols, N., Headd, J.J., Hung, L.-W., Kapral, G.J., Grosse-Kunstleve, R.W., et al. (2010). PHENIX: a comprehensive Python-based system for macromolecular structure solution. Acta.Crystallogr. Sect. D *66*, 213–221.

Bentmann, E., Neumann, M., Tahirovic, S., Rodde, R., Dormann, D., and Haass, C. (2012). Requirements for stress granule recruitment of fused in sarcoma (FUS) and TAR DNA-binding protein of 43 kDa (TDP-43). J. Biol. Chem. *287*, 23079–23094.

Cao, Q., Boyer, D.R., Sawaya, M.R., Ge, P., and Eisenberg, D.S. (2019). Cryo-EM structures of four polymorphic TDP-43 amyloid cores. Nat. Struct. Mol. Biol. *26*, 619–627.

Colombrita, C., Zennaro, E., Fallini, C., Weber, M., Sommacal, A., Buratti, E., Silani, V., and Ratti, A. (2009). TDP-43 is recruited to stress granules in conditions of oxidative insult. J. Neurochem. *111*, 1051–1061.

Deng, Q., Holler, C.J., Taylor, G., Hudson, K.F., Watkins, W., Gearing, M., Ito, D., Murray, M.E., Dickson, D.W., and Seyfried, N.T. (2014). FUS is phosphorylated by DNA-PK and accumulates in the cytoplasm after DNA damage. J. Neurosci. *34*, 7802–7813.

Ding, X., Sun, F., Chen, J., Chen, L., Tobin-Miyaji, Y., Xue, S., Qiang, W., and Luo, S.-Z. (2020). Amyloid-forming segment induces aggregation of FUS-LC domain from phase separation modulated by site-specific phosphorylation. J. Mol. Biol. *432*, 467–483.

Dobson, C.M., Knowles, T.P.J., and Vendruscolo, M. (2020). The amyloid phenomenon and its significance in biology and medicine. Cold Spring Harb. Perspect.Biol. *12*, a033878.

Eisenberg, D., and Jucker, M. (2012). The amyloid state of proteins in human diseases. Cell *148*, 1188–1203.

Eisenberg, D.S., and Sawaya, M.R. (2017). Structural studies of amyloid proteins at the molecular level. Annu. Rev. Biochem. *86*, 69–95.

Emsley, P., Lohkamp, B., Scott, W.G., and Cowtan, K. (2010). Features and development of coot. Acta Crystallogr. D *66*, 486–501.

Fitzpatrick, A.W.P., Falcon, B., He, S., Murzin, A.G., Murshudov, G., Garringer, H.J., Crowther, R.A., Ghetti, B., Goedert, M., and Scheres, S.H.W. (2017). Cryo-EM structures of tau filaments from Alzheimer's disease. Nature *547*, 185–190.

Fujii, R., Okabe, S., Urushido, T., Inoue, K., Yoshimura, A., Tachibana, T., Nishikawa, T., Hicks, G.G., and Takumi, T. (2005). The RNA binding protein TLS is translocated to dendritic spines by mGluR5 activation and regulates spine morphology. Curr. Biol. *15*, 587–593.

Gambetti, P., Cali, I., Notari, S., Kong, Q., Zou, W.-Q., and Surewicz, W.K. (2011). Molecular biology and pathology of prion strains in sporadic human prion diseases. Acta.Neuropathol. *121*, 79–90.

Gasset-Rosa, F., Lu, S., Yu, H., Chen, C., Melamed, Z.E., Guo, L., Shorter, J., Da Cruz, S., and Cleveland, D.W. (2019). Cytoplasmic TDP-43 de-mixing independent of stress granules drives inhibition of nuclear import, loss of nuclear TDP-43, and cell death. Neuron *102*, 339–357.

Gremer, L., Schölzel, D., Schenk, C., Reinartz, E., Labahn, J., Ravelli, R.B.G., Tusche, M., Lopez-Iglesias, C., Hoyer, W., and HEISE, H. (2017). Fibril structure of amyloid-β (1–42) by cryo–electron microscopy. Science *358*, 116–119.

Guenther, E.L., Cao, Q., Trinh, H., Lu, J., Sawaya, M.R., Cascio, D., Boyer, D.R., Rodriguez, J.A., Hughes, M.P., and Eisenberg, D.S. (2018). Atomic structures of TDP-43 LCD segments and insights into reversible or pathogenic aggregation. Nat. Struct. Mol. Biol. *25*, 463–471.

Gui, X., Luo, F., Li, Y., Zhou, H., Qin, Z., Liu, Z., Gu, J., Xie, M., Zhao, K., and Dai, B. (2019). Structural basis for reversible amyloids of hnRNPA1 elucidates their role in stress granule assembly. Nat. Commun. *10*, 1–12.

Hughes, M.P., Sawaya, M.R., Boyer, D.R., Goldschmidt, L., Rodriguez, J.A., Cascio, D., Chong, L., Gonen, T., and Eisenberg, D.S. (2018). Atomic structures of low-complexity protein segments reveal kinked β sheets that assemble networks. Science *359*, 698–701.

Iadanza, M.G., Jackson, M.P., Hewitt, E.W., Ranson, N.A., and Radford, S.E. (2018). A new era for understanding amyloid structures and disease. Nat. Rev. Mol. Cell Biol. *19*, 755–773.

Ju, S., Tardiff, D.F., Han, H., Divya, K., Zhong, Q., Maquat, L.E., Bosco, D.A., Hayward, L.J., Brown, R.H., JR., and Lindquist, S. (2011). A yeast model of FUS/TLS-dependent cytotoxicity. PLoS Biol. *9*, e1001052.

Jucker, M., and Walker, L.C. (2013). Self-propagation of pathogenic protein aggregates in neurodegenerative diseases. Nature *501*, 45–51.

Kam, T.-I., Mao, X., Park, H., Chou, S.-C., Karuppagounder, S.S., Umanah, G.E., Yun, S.P., Brahmachari, S., Panicker, N., and Chen, R. (2018). Poly (ADP-ribose) drives pathologic α-synuclein neurodegeneration in Parkinson's disease. Science. *362*, eaat8407.

Kato, M., Han, T.W., Xie, S., Shi, K., Du, X., Wu, L.C., Mirzaei, H., Goldsmith, E.J., Longgood, J., and Pei, J. (2012). Cell-free formation of RNA granules: low complexity sequence domains form dynamic fibers within hydrogels. Cell *149*, 753–767.

Kim, H.J., Kim, N.C., Wang, Y.-D., Scarborough, E.A., Moore, J., Diaz, Z., Maclea, K.S., Freibaum, B., Li, S., and Molliex, A. (2013). Mutations in prion-like domains in hnRNPA2B1 and hnRNPA1 cause multisystem proteinopathy and ALS. Nature *495*, 467–473.

Lagier-Tourenne, C., Polymenidou, M., Hutt, K.R., Vu, A.Q., Baughn, M., Huelga, S.C., Clutario, K.M., Ling, S.-C., Liang, T.Y., and Mazur, C. (2012). Divergent roles of ALS-linked proteins FUS/TLS and TDP-43 intersect in processing long pre-mRNAs. Nat. Neurosci. *15*, 1488–1497.

Lee, M., Ghosh, U., Thurber, K.R., Kato, M., and Tycko, R. (2020). Molecular structure and interactions within amyloid-like fibrils formed by a low-complexity protein sequence from FUS. Nat. Commun. *11*, 1–14.

Li, D., and Liu, C. (2021). Hierarchical chemical determination of amyloid polymorphs in neurodegenerative disease. Nat. Chem. Biol. *17*, 237–245.

Li, Y., Zhao, C., Luo, F., Liu, Z., Gui, X., Luo, Z., Zhang, X., Li, D., Liu, C., and Li, X. (2018). Amyloid fibril structure of α-synuclein determined by cryo-electron microscopy. Cell Res. *28*, 897–903.

Ling, S.-C., Polymenidou, M., and Cleveland, D.W. (2013). Converging mechanisms in ALS and FTD: disrupted RNA and protein homeostasis. Neuron *79*, 416–438.

Luo, F., Gui, X., Zhou, H., Gu, J., Li, Y., Liu, X., Zhao, M., Li, D., Li, X., and Liu, C. (2018). Atomic structures of FUS LC domain segments reveal bases for reversible amyloid fibril formation. Nat. Struct. Mol. Biol. *25*, 341–346.

March, Z.M., King, O.D., and Shorter, J. (2016). Prion-like domains as epigenetic regulators, scaffolds for subcellular organization, and drivers of neurodegenerative disease. Brain Res. *1647*, 9–18.

Martin, E.W., Holehouse, A.S., Peran, I., Farag, M., Incicco, J.J., Bremer, A., Grace, C.R., Soranno, A., Pappu, R.V., and Mittag, T. (2020). Valence and patterning of aromatic residues determine the phase behavior of prion-like domains. Science *367*, 694–699.

Molliex, A., Temirov, J., Lee, J., Coughlin, M., Kanagaraj, A.P., Kim, H.J., Mittag, T., and Taylor, J.P. (2015). Phase separation by low complexity domains promotes stress granule assembly and drives pathological fibrillization. Cell *163*, 123–133.

Murakami, T., Qamar, S., Lin, J.Q., Schierle, G.S.K., Rees, E., Miyashita, A., Costa, A.R., Dodd, R.B., Chan, F.T.S., and Michel, C.H. (2015). ALS/FTD mutation-induced phase transition of FUS liquid droplets and reversible hydrogels into irreversible hydrogels impairs RNP granule function. Neuron *88*, 678–690.

Murray, D.T., Kato, M., Lin, Y., Thurber, K.R., Hung, I., Mcknight, S.L., and Tycko, R. (2017). Structure of FUS protein fibrils and its relevance to self-assembly and phase separation of low-complexity domains. Cell *171*, 615–627.

Murray, D.T., and Tycko, R. (2020). Side chain hydrogen-bonding interactions within amyloid-like fibrils formed by the low-complexity domain of FUS: evidence from solid state nuclear magnetic resonance spectroscopy. Biochemistry *59*, 364–378.

Paravastu, A.K., Leapman, R.D., Yau, W.-M., and Tycko, R. (2008). Molecular structural basis for polymorphism in Alzheimer's β-amyloid fibrils. Proc. Natl. Acad. Sci. U S A *105*, 18349–18354.

Patel, A., Lee, H.O., Jawerth, L., Maharana, S., Jahnel, M., Hein, M.Y., Stoynov, S., Mahamid, J., Saha, S., and Franzmann, T.M. (2015). A liquid-to-solid phase transition of the ALS protein FUS accelerated by disease mutation. Cell *162*, 1066–1077.

Peng, C., Gathagan, R.J., Covell, D.J., Medellin, C., Stieber, A., Robinson, J.L., Zhang, B., Pitkin, R.M., Olufemi, M.F., and Luk, K.C. (2018). Cellular milieu imparts distinct pathological α-synuclein strains in α-synucleinopathies. Nature *557*, 558–563.

Peng, C., Trojanowski, J.Q., and Lee, V.M.Y. (2020). Protein transmission in neurodegenerative disease. Nat. Rev. Neurol. *16*, 199–212.

Pettersen, E.F., Goddard, T.D., Huang, C.C., Couch, G.S., Greenblatt, D.M., Meng, E.C., and Ferrin, T.E. (2004). UCSF Chimera—a visualization system for exploratory research and analysis. J. Comput. Chem. *25*, 1605–1612.

Polymenidou, M., Lagier-Tourenne, C., Hutt, K.R., Bennett, C.F., Cleveland, D.W., and Yeo, G.W. (2012). Misregulated RNA processing in amyotrophic lateral sclerosis. Brain Res. *1462*, 3–15.

Portz, B., Lee, B.L., and Shorter, J. (2021). FUS and TDP-43 phases in health and disease. Trends Biochem.Sci. *46*, 550–563.

Purice, M.D., and Taylor, J.P. (2018). Linking hnRNP function to ALS and FTD pathology. Front. Neurosci. *12*, 326.

Qiang, W., Yau, W.-M., Lu, J.-X., Collinge, J., and Tycko, R. (2017). Structural variation in amyloid-β fibrils from Alzheimer's disease clinical subtypes. Nature *541*, 217–221.

Rhoads, S.N., Monahan, Z.T., Yee, D.S., Leung, A.Y., Newcombe, C.G., O'meally, R.N., Cole, R.N., and Shewmaker, F.P. (2018). The prionlike domain of FUS is multiphosphorylated following DNA damage without altering nuclear localization. Mol. Biol. Cell. *29*, 1786–1797.

Rohou, A., and Grigorieff, N. (2015). CTFFIND4: fast and accurate defocus estimation from electron micrographs. J. Struct. Biol. *192*, 216–221.

Sawaya, M.R., Hughes, M.P., Rodriguez, J.A., Riek, R., and Eisenberg, D.S. (2021). The expanding amyloid family: structure, stability, function, and pathogenesis. Cell *184*, 4857–4873.

Scheres, S.H.W. (2020). Amyloid structure determination in RELION-3.1. Acta Crystallogr. D Struct. Biol. *76*, 94–101.

Schwartz, J.C., Ebmeier, C.C., Podell, E.R., Heimiller, J., Taatjes, D.J., and Cech, T.R. (2012). FUS binds the CTD of RNA polymerase II and regulates its phosphorylation at Ser2. Genes Dev. *26*, 2690–2695.

Schweighauser, M., Shi, Y., Tarutani, A., Kametani, F., Murzin, A.G., Ghetti, B., Matsubara, T., Tomita, T., Ando, T., and Hasegawa, K. (2020). Structures of α-synuclein filaments from multiple system atrophy. Nature *585*, 464–469.

Shi, Y., Zhang, W., Yang, Y., Murzin, A.G., Falcon, B., Kotecha, A., Van Beers, M., Tarutani, A., Kametani, F., and Garringer, H.J. (2021). Structure-based classification of tauopathies. Nature *598*, 359–363.

Soto, C., and Pritzkow, S. (2018). Protein misfolding, aggregation, and conformational strains in neurodegenerative diseases. Nat. Neurosci. *21*, 1332–1340.

Sun, Y., Zhao, K., Xia, W., Feng, G., Gu, J., Ma, Y., Gui, X., Zhang, X., Fang, Y., and Sun, B. (2020). The nuclear localization sequence mediates hnRNPA1 amyloid fibril formation revealed by cryoEM structure. Nat. Commun. *11*, 1–8.

Vaquer-Alicea, J., and Diamond, M.I. (2019). Propagation of protein aggregation in neurodegenerative diseases. Annu. Rev. Biochem. *88*, 785–810.

Wang, L.-Q., Zhao, K., Yuan, H.-Y., Wang, Q., Guan, Z., Tao, J., li, X.-N., Sun, Y., Yi, C.-W., and Chen, J. (2020). Cryo-EM structure of an amyloid fibril formed by full-length human prion protein. Nat. Struct. Mol. Biol. *27*, 598–602.

Wang, W.-Y., Pan, L., Su, S.C., Quinn, E.J., Sasaki, M., Jimenez, J.C., Mackenzie, I.R.A., Huang, E.J., and Tsai, L.-H. (2013). Interaction of FUS and HDAC1 regulates DNA damage response and repair in neurons. Nat. Neurosci. *16*, 1383–1391.

Wang, X., Arai, S., Song, X., Reichart, D., Du, K., Pascual, G., Tempst, P., Rosenfeld, M.G., Glass, C.K., and Kurokawa, R. (2008). Induced ncRNAs allosterically modify RNA-binding proteins in cis to inhibit transcription. Nature *454*, 126–130.

Yang, L., Gal, J., Chen, J., and Zhu, H. (2014). Self-assembled FUS binds active chromatin and regulates gene transcription. Proc. Natl. Acad. Sci. *111*, 17809–17814.

Zheng, S.Q., Palovcak, E., Armache, J.P., Verba, K.A., Cheng, Y., and Agard, D.A. (2017). MotionCor2: anisotropic correction of beam-induced motion for improved cryo-electron microscopy. Nat. Methods *14*, 331–332.

STAR★METHODS

KEY RESOURCES TABLE

REAGENT or RESOURCE	SOURCE	IDENTIFIER
Bacterial and virus strains		
BL21 (DE3) *E. coli*	TransGenBiotech	Cat#CD601-03
Chemicals, peptides, and recombinant proteins		
mCerulean-FUS LC	This study	N/A
Critical commercial assays		
Cell Counting Kit-8	Yeasen Biotechnology (Shanghai) Co., Ltd.	Cat#40203ES76
Deposited data		
FUS LC fibril core, type III, coordinate	This paper	PDB: 7VQQ
FUS LC fibril core, type III, cryo-EM map	This paper	EMD: 32092
FUS RAC1, coordinate	(Luo et al., 2018)	PDB: 5XSG
FUS RAC2, coordinate	(Luo et al., 2018)	PDB: 5XRR
FUS LC fibril core, type I, coordinate	(Murray et al., 2017)	PDB: 5W3N
FUS LC fibril core, type II, coordinate	(Lee et al., 2020)	PDB: 6XFM
See Data and code availability section		
Experimental models: Cell lines		
HEK-293T	ATCC	ATCC® CRL-3216, RRID: CVCL_0063
Software and algorithms		
ImageJ	NIH	https://imagej.nih.gov/ij/
GraphPad Prism Software	GraphPad	https://www.graphpad.com/scientificsoftware/prism/
MotionCor2	(Zheng et al., 2017)	https://emcore.ucsf.edu/ucsf-software
CTFFIND	(Rohou and Grigorieff, 2015)	https://grigoriefflab.umassmed.edu/ctffind4
RELION	(Scheres, 2020)	https://www3.mrc-lmb.cam.ac.uk/relion
COOT	(Emsley et al., 2010)	https://www2.mrc-lmb.cam.ac.uk/personal/pemsley/coot/
PHENIX	(Adams et al., 2010)	https://phenix-online.org/documentation/reference/real_space_refine.html
UCSF Chimera	(Pettersen et al., 2004)	https://www.cgl.ucsf.edu/chimera/

RESOURCE AVAILABILITY

Lead contact

Further information and requests for resources should be directed to and will be fulfilled by the lead contact Cong Liu (liulab@sioc.ac.cn).

Materials availability

Reagents generated in this study will be available upon request.

Data and code availability

- The cryo-EM density map and corresponding atomic model generated in this work have been deposited at the EMDB database and PDB database and are publicly available as of the date of publication. Accession numbers are listed in the key resources table.
- This paper analyzes existing, publicly available data. These accession numbers for the datasets are listed in the key resources table. These accession numbers of 100 existing atomic models analyzed in Figure 5

from PDB database are listed as below: 5O3L, 5O3O, 5O3T, 5OQV, 6HRE, 6HRF, 6A6B, 6H6B, 6GK3, 6GX5, 6CU7, 6CU8, 6QJH, 6QJM, 6QJP, 6QJQ, 6SSX, 6SST, 6SDZ, 6OSJ, 6OSM, 6OSL, 6R4R, 6SHS, 6IC3, 6HUD, 6NWP, 6NWQ, 6N37, 6N3B, 6N3A, 6N3C, 6VHA, 6VH7, 6VHL, 6VI3, 6LRQ, 7BX7, 6TJO, 6TJX, 6XYO, 6XYP, 6XYQ, 6WQK, 6L4S, 6XFM, 6VW2, 6UUR, 6LNI, 6Y1A, 6ZRF, 6ZRQ, 6ZRR, 6PEO, 6PES, 6L1T, 6L1U, 6UFR, 6VPS, 7MKF, 7MKG, 7MKH, 7LNA, 7NCA, 7NCG, 7NCH, 7NCI, 7NCJ, 7NCK, 6ZCF, 6ZCG, 6ZCH, 6Z1O, 6Z1I, 7KWZ, 7M61, 7M62, 7M64, 7M65, 6W0O, 7DA4, 7DWV, 7LC9, 7E0F, 7C1D, 7P6A, 7P6B, 7P6C, 7P6D, 7P6E, 7P65, 7P66, 7P67, 7P68, 7NRS, 7NRT, 7NRQ, 7NRV, 7NRX, 7VQQ.

- This paper does not report original code.
- Any additional information required to reanalyze the data reported in this paper is available from the lead contact upon request.

METHOD DETAILS

Purification of recombinant mCerulean-FUS LC

The gene encoding FUS LC (residues 2–214) was inserted into pET22b vector with a His-tagged mCerulean at the N terminus. mCerulean-FUS LC was overexpressed in Escherichia coli BL21 (DE3) at 25°C overnight after induction by 0.5 mM isopropyl-1-thio-D-galactopyranoside (IPTG). Then, cells were collected by centrifugation and lysed in the lysis buffer (50mM Tris-HCl, pH 7.5, 500 mM NaCl, 4 mM β-mercaptoethanol and 2 mM Phenylmethylsulfonyl fluoride) at 4°C. Cell lysate was sonicated, followed by centrifugation at 30,966 × g for 45 min at 4°C. The supernatant was loaded into Ni column (HisTrap FF, GE Healthcare) and mCerulean-FUS LC protein was eluted with the elution buffer consisting of 50mM Tris-HCl, pH 7.5, 500 mM NaCl, 500 mM imidazole and 4 mM β-mercaptoethanol. The protein was further fractionated by Superdex 75 (GE Healthcare) in 50mM Tris-HCl, pH 7.5, 100 mM NaCl and 5% glycerol.

Fluorescence recovery after photo bleaching (FRAP) assay and fibril formation

The PFRP assay was performed using the FRAP mode of the Leica SP8 confocal microscopy system with a 100× oil objective. In brief, 100 μM mCerulean-FUS-LC in the buffer containing 50mM Tris-HCl, pH 7.5, 100 mM NaCl, 2% glycerin and 10% Dextran 70 were incubated at 37°C for 0 h and 24h. A circular region of interest (ROI) approximately 2 μm in diameter was bleached for 2.5 s using a full power 405 nm laser. After bleaching, time-lapse images were captured. For each indicated time point (t), the fluorescence intensity of ROI was corrected by the intensity of a neighboring unbleached region. The fluorescence intensity of pre-bleaching was set to 100% and the fluorescence intensity at each time point (It) was used to calculate the fluorescence recovery (FR) according to the following formula: FR(t) = It/Ipre-bleaching. Image J was used for quantification and GraphPad Prism to plot and analyze the FRAP experiments. 100 μM mCerulean-FUS-LC in the buffer containing 50mM Tris-HCl, pH 7.5, 100 mM NaCl, and 2% glycerin was incubated at 37°C for 5 days and harvested for cryo-EM fibril sample preparation.

Cell viability assay

HEK293T cells were cultured to test the cytotoxicity of FUS LC fibrils with Cell Counting Kit-8 (CCK-8) kit. FUS LC fibrils was sonicated at 20% power for 15 times (1 s per time, 1 s per interval) on ice by JY92-IIN sonicator. HEK293T cells cultured in 96-well plate were treated with sonicated FUS LC fibrils at final concentrations of 5 and 10 μM for 24 h. Then cell viability was tested with Cell Counting Kit-8 kit following the manufacturer's protocol. Briefly, CCK-8 solution (10 μl/well) was added to each well. The absorbance of plate was measured at 450 nm after incubating for 30 min. The data was analyzed with GraphPad Prism 6.

Negative-staining transmission electron microscopy

A drop of 5 μl of FUS LC fibril samples was loaded onto a glow-discharged, carbon-coated, 200 mesh copper grid (Beijing Zhongjingkeyi Technology Co., Ltd.). The grid was held for 45s and washed by absorbing a drop of double-distilled water and a drop of 3% uranyl acetate, respectively. The grid was then stained with a drop of 3% uranyl acetate for another 45 s and dried in air. The images were captured by a Tecnai T12 microscope (FEI).

Cryo-EM data collection

Holey carbon copper Quantifoil grids (R2/1, 300 mesh) were used to prepare cryo-EM samples. Grid with a drop of 4 μl of FUS LC fibril samples loaded on, was plunge-frozen in liquid ethane using Vitrobot Mark IV(FEI) and transferred to Titan Krios transmission electron microscope (Thermo Fisher Scientific) operated

at 300 kV. Cryo-EM micrographs with a defocus from −2 to −1 μm were captured with a Gatan K2 direct detector in super-resolution mode. 32 movies per micrograph were recorded with a pixel size of 1.1 Å pixel^{-1} using a dose of 40 e^{-}Å^{-2}. Automated cryo-EM data collection was performed with EPU software (Thermo Fisher Scientific).

Imaging processing, reconstruction, and model building

32 movie frames were processed using MotionCorr2 to correct beam induced with dose weighting and stacked(Zheng et al., 2017). CTFFIND4.1.8 was then used to estimate the contrast transfer function(Rohou and Grigorieff, 2015). Manual picking method of RELION3.1 was used to picked filaments manually and RELION 3.1 was used to carry out subsequent steps of helical reconstruction.

16,394 fibrils from 1,089 micrographs were selected and manually picked for further processing. Fibrils were first extracted using 1,024-pixel box size with an inter-box distance of 113 Å and only one dominant specie of twist fibril with a population of over 99% was identified according to the reference-free 2D classification using segments with a 1,024-pixel box size. 256-pixel box size with an inter-box distance of 28 Å was then applied to extracted segments for further 2D classification and segments comprising an entire helical crossover were selected. An initial 3D reference was de novo generated with suitable 2D class averages by relion_helix_inimodel2d, low-pass filtered to 60 Å and applied as reference to perform 3D classification. 3D jobs with K = 3 were performed to select homogenous segments. Local optimization of helical twist and rise was carried out to optimize twist parameters once separated β-strands were clearly shown. A final reconstruction with Refine3D was performed with selected segments. The final overall resolution estimate was calculated to be 2.9 Å based on the map–map Fourier shell correlation (FSC) at 0.143 cutoff with a soft-edge solvent mask and noise substitution PostProcess.

Atomic model building

Solid state NMR structure of FUS LC fibril (PDB: 5W3N) was used as initial model. The model was built into the central region of the electron density map in COOT(Emsley et al., 2010). A 3-layer model was generated and refined by real_space_refine program in PHENIX(Adams et al., 2010).

QUANTIFICATION AND STATISTICAL ANALYSIS

One-way ANOVA followed by Tukey HSD post hoc test was performed in the GraphPad Prism software following standard procedures.